

Unveiling Mysteries of GdRu_2Si_2 : The Impact of Interlayer Coupling on The Magnetic Response

Sagar Sarkar,¹ Rohit Pathak,¹ Anna Delin,^{2,3,4} Olle Eriksson,^{1,5} and Vladislav Borisov¹

¹*Department of Physics and Astronomy,
Uppsala University, Uppsala, 751 20, Sweden.*

²*Department of Applied Physics, School of Engineering Sciences, KTH Royal
Institute of Technology, AlbaNova University Center, SE-10691 Stockholm, Sweden*

³*Wallenberg Initiative Materials Science for Sustainability (WISE),
KTH Royal Institute of Technology, SE-10044 Stockholm, Sweden*

⁴*SeRC (Swedish e-Science Research Center), KTH Royal
Institute of Technology, SE-10044 Stockholm, Sweden*

⁵*Wallenberg Initiative Materials Science for Sustainability,
Uppsala University, 75121 Uppsala, Sweden.*

Abstract

GdRu₂Si₂ has recently drawn significant attention as a centrosymmetric magnet capable of hosting a short-period skyrmion square lattice (SkL) in the absence of Dzyaloshinskii–Moriya interaction (DMI). In this system, Gd atoms are arranged on a square lattice forming 2D layers separated by the Ru-Si network in the out-of-plane direction. In the low T regime, the ground state for zero/smaller external magnetic field (\mathbf{B}_\perp) along the out-of-plane direction is a single helical state, characterized by one modulation vector \vec{Q} along one of the in-plane directions of the square lattice. For some critical range of higher \mathbf{B}_\perp , the helical state transforms into a SkL state that can be viewed as the overlap of two helical states defined with \vec{Q} vectors in two in-plane directions, with the same magnitude of \vec{Q} as for the single helical state. So far in the literature, importance has been given to this in-plane \vec{Q} vector in understanding the magnetic phases of the system, considering the out-of-plane magnetic coupling to be weak, which therefore has been ignored. Our calculation of the Gd-Gd magnetic exchange interactions (J_{ij}) however shows the strongest J_{ij} to occur between second neighbour Gd atoms along the [111] body-diagonal direction of the unit cell. This along with the body-centred tetragonal structure of the Gd sublattice points to the presence of a hitherto ignored modulation vector, $\vec{Q}_{[111]}$, along the [111] direction in the helical ground state. We demonstrate from Atomistic Spin Dynamics (ASD) simulations the importance of this interaction. This interlayer modulation vector $\vec{Q}_{[111]}$, along with the intralayer $\vec{Q}_{[100]}$, determines the total magnetic ordering of the system. As shown here, $\vec{Q}_{[111]}$ cannot be ignored while simulating the magnetic phase diagram with ASD, since a simulation cell that does not consider $\vec{Q}_{[111]}$, fails to reproduce the experimentally observed magnetic phase transitions with \mathbf{B}_\perp . Our data shows that the magnetic phases in GdRu₂Si₂ are far more complex than what has been previously discussed. Although the system looks like a layered one, which can potentially give rise to symmetric anisotropic exchange and Kitaev-like interactions, it is in reality a strong 3D magnet demanding additional considerations to be made for its theoretical modelling. Our work provides a better understanding of the complex magnetism of GdRu₂Si₂. Similar important interlayer effects may be present also in many other layered magnetic systems.

I. INTRODUCTION

GdRu₂Si₂ is a magnetic metallic system that has recently attracted attention, along with some analogous systems, due to its interesting magnetic properties. The main source of magnetism here are the localized half-filled Gd *4f* orbitals resulting in a large spin moment of $7\mu_B$ [1]. The delocalized Gd *5d* and Ru *4d* states, on the other hand, create a pool of conduction electrons leading to metallicity and magnetic exchange interactions between the Gd *4f* moments via the RKKY mechanism [2]. Though Gd is a relatively heavy element, with anticipated large spin-orbit effects, the presence of inversion symmetry forbids the emergence of Dzyaloshinskii–Moriya interaction (DMI) [3,4] which is a widely discussed chiral interaction. As a result, the Heisenberg exchange becomes the dominant mechanism of spin-spin interactions which may potentially provide non-collinear textures in GdRu₂Si₂, as we will investigate in detail in this work. Like any magnetic system, the magnetic properties of GdRu₂Si₂ depend on the temperature (T) and external magnetic field (B). This particular system, however, shows an interesting and rich $B - T$ phase diagram consisting of different phases [5]. The primary interest is the square skyrmion Lattice (SkL) phase that appears in the low- T regime within a narrow range of external magnetic field around 2 T.

Magnetic skyrmions are topological solitons with a topological charge defined by the so-called skyrmion number N_{sk} [6]. The spin ordering in a skyrmion can be considered as a special arrangement of 3D spins on a 2D plane in such a manner that they could be mapped back on the surface of a sphere [6, 7]. A periodic arrangement of these skyrmions is referred to as a skyrmion crystal (SkX) that shows unconventional magnetic and transport properties [7–11]. This makes them promising candidates for future memory devices and spintronics applications [12]. A SkX is not something new and has previously been observed in chiral magnets [13] like MnSi, FeGe, and Cu₂OSeO₃ [14–19]. In these chiral magnets, the non-collinearity of the spins in the SkX results from a competition between exchange and DMI leading to skyrmions with a large size between 20 and 100 nm [20, 21].

What makes GdRu₂Si₂ special compared to these known skyrmionic systems is that the SkL results mainly from exchange frustration without DMI [13, 22]. This results in much smaller-sized skyrmions of around 2 nm in the SkL phase [5, 22]. The smaller size of these topological objects theoretically means higher surface density and better device applicability, although single skyrmions not arranged in a lattice, which would be necessary

for applications, were not yet observed in GdRu_2Si_2 . Hence, the ongoing efforts aim to understand, from a fundamental point of view, the magnetic properties of this system. This would aid in tuning the position of the SkL phase in the $B - T$ phase diagram. This is part of an emerging field of scientific research with the goal to understand the microscopic electronic and magnetic properties behind the stabilization of the SkL phase in systems without DMI. The SkL phase in GdRu_2Si_2 , appearing for some values of external magnetic field, is characterized by a double- \mathbf{Q} modulation of the Gd spin texture. In contrast, the zero- and low-field helical spiral state can be described by a single \mathbf{Q} vector. As discussed in the literature, the microscopic origin of this helimagnetic state is the exchange frustration due to the RKKY mechanism [2]. To obtain a quantitative understanding of the exchange frustration, Nomoto *et al.* [13] performed an orbital decomposition of the calculated Gd-Gd exchange J_{ij} . The Fourier transform $J(q)$ of the orbital-decomposed exchange revealed an FM and AFM ground state for the $5d - 5d$ and $4f - 4f$ components, respectively. The presence of these competing interactions was claimed to be the reason for noncollinearity due to exchange frustration. This claim, however, raises a question, since competition between the orbital-specific exchange interactions between two Gd atoms would not lead to a non-collinear order between them, because the dominant orbital component of Heisenberg exchange related to Gd- $5d$ states favors a collinear order.

Getting back to the phase diagram and stabilization of the critical double- \mathbf{Q} SkL phase, additional mechanisms were suggested along with the exchange frustration. The importance of four-spin (biquadratic) interaction mediated by itinerant electrons in the presence of an easy axis anisotropy has been claimed from the very beginning [5, 23]. It should be noted that four-spin interactions are often discussed for itinerant magnets, as they are the lowest-order interactions beyond the Heisenberg exchange that can be significant enough to affect the magnetic order. However, a recent theoretical study by Boujziz *et al.* [22] reported the stability of the SkL phase in this system without four-spin interactions. According to this study, the double- \mathbf{Q} SkL arises from the combination of crystal symmetry-dependent frustrated RKKY interactions with a uniaxial magnetocrystalline anisotropy (K_U) and a magnetic field perpendicular to the helical axis. Though a consensus has not yet been achieved as to what drives the skyrmion formation, there is a general agreement regarding the characterization of different magnetic phases in terms of the modulation vectors. The two in-plane modulation vectors \mathbf{Q}_{100} along \mathbf{a} -axis and \mathbf{Q}_{010} along \mathbf{b} -axis have been considered

to describe the magnetic states. The helical ground state at zero or low external field (B) requires either \mathbf{Q}_{100} or \mathbf{Q}_{010} . The critical SkL requires, however, the simultaneous presence of both \mathbf{Q}_{100} and \mathbf{Q}_{010} . These two vectors are enough to describe the magnetic phases as they appear and have been observed in each of the two-dimensional (2D) Gd square-lattice layers.

In this report, we calculate and analyze in detail the magnetic exchange interactions in this layered rare-earth system GdRu_2Si_2 . We show that the magnetic phases are more complex than what was discussed in the literature so far and cannot be described with the in-plane modulation vectors alone. The calculated exchange interactions indicate, for example, that the exchange frustration results from competition between the intralayer and interlayer exchange, where the latter was mostly neglected in the previous studies. A stronger interlayer FM exchange along with the body-centred tetragonal Gd sublattice results in an interlayer modulation vector \mathbf{Q}_{111} along the [111] body-diagonal direction of the unit cell which we confirm using atomistic spin dynamics (ASD) simulations. The \mathbf{Q}_{111} modulation of the spin texture cannot be neglected while simulating the magnetic phase diagram, since ASD simulation for a supercell incompatible with \mathbf{Q}_{111} does not show the experimentally observed magnetic phase transitions as a function of applied magnetic field \mathbf{B} . Our results also strongly suggest that the Heisenberg exchange and uniaxial anisotropy alone cannot stabilize a SkL phase and, for that reason, other magnetic interactions acting as a perturbation might become important.

While our work is about a concrete magnetic system, the discussion of magnetic phases and theoretical approaches for their simulation is quite general and can be applied to many other non-collinear magnets with spiral or skyrmion phases. In particular, using GdRu_2Si_2 as an example we point out some important aspects of methodology which are required in order to model correctly the magnetic phase diagram using atomistic spin dynamics (ASD). Since ASD is widely used nowadays for studying magnets, the methodological conclusions of our study can make a useful contribution to the field in general. It is also worthwhile to mention that GdRu_2Si_2 has a very common type of crystal structure, the so-called 122- or ThCr_2Si_2 -type of structure, which is also found in widely discussed iron-based superconductors and magnets [24] and rare-earth magnets LnRh_2Si_2 with ultrafast demagnetization dynamics [25] (see further examples in [26]).

II. METHODOLOGY

A. Electronic structure and Magnetic exchange

We have considered the two-formula unit tetragonal unit cell for our system. The lattice parameters were kept fixed at the experimental values [27]. First, we have calculated the electronic structure from density functional theory (DFT) using a projected augmented wave (PAW) method [28, 29] as implemented in the Vienna ab-initio simulation package (VASP) [30–33]. The generalized gradient approximation (GGA) [34] in the Perdew-Burke-Ernzerhof (PBE) parametrization [34, 35] was considered for the exchange-correlation functional and a plane-wave energy cutoff of 500 eV was used for the basis set. Along with this, a Γ -centered Monkhorst-Pack $20 \times 20 \times 10$ \mathbf{k} -mesh, providing convergence of the total energy and local moments, was used for reciprocal space integration. The main purpose was to check the effect of the crystalline environment and other delocalized s , p , and d states on the atomic-like localized Gd $4f$ states. For this, the Gd $4f$ states were considered as part of the valence electronic manifold, and to achieve a correct description of their localized nature we have performed a DFT+ U calculation within the Hartree-Fock approximation [36, 37]. For this, the rotationally invariant formulation of Liechtenstein *et al.* [38] was used with the Coulomb interaction parameters $U = 6.7$ eV and $J = 0.7$ eV on the Gd $4f$ states, based on a previous study [39]. Calculations based on this methodology were used here for an initial analysis of electronic properties presented also in Fig. 2.

Following this, to extract the magnetic exchange interactions between the Gd moments, the electronic structure was again calculated with the Full Potential Linear Muffin-Tin Orbital (FP-LMTO) method, as implemented in the Relativistic Spin-Polarized Toolkit (RSPT) [40–43]. GGA-PBE exchange-correlation functional was used similarly to the VASP calculations. These calculations included two sets of basis functions, covering both valence and semi-core states. These states were specifically constructed from the $6s$, $6p$, and $5d$ orbitals for Gd and Ru, and the $3s$, $3p$, and $3d$ orbitals for Se respectively. The Gd $4f$ states were considered in the core to be treated scalar relativistically to reduce the computational cost. Hence, a DFT+ U calculation was not required in this case. We chose kinetic tail energies as -0.1 , -2.3 , and 1.5 Ry. For the Brillouin zone sampling, we used an optimized γ -centered Monkhorst-Pack mesh of $32 \times 32 \times 16$ \mathbf{k} -points. From here, the *ab-initio* Kohn-Sham Hamil-

tonian or the DFT Hamiltonian is mapped onto an effective Heisenberg Hamiltonian with classical spins of the following form [44, 45] to extract the interatomic exchange interactions through the application of the magnetic force theorem (MFT) [44, 46] (for a review, see Ref. [47]):

$$H = - \sum_{i \neq j} J_{ij} \vec{e}_i \cdot \vec{e}_j. \quad (1)$$

Here, (i, j) are the indices for the magnetic sites in the system, while \vec{e}_i and \vec{e}_j are the unit vectors along the spin directions at sites i , and j respectively; J_{ij} is the exchange interaction between the two spins at sites i and j . In the Green-function-based approach to evaluate the J_{ij} values, used in the RSPt software, the exchange parameters J_{ij} are determined from a generalized non-relativistic expression as given below [45].

$$J_{ij} = \frac{T}{4} \sum_n \text{Tr} \left[\hat{\Delta}_i(i\omega_n) \hat{G}_{ij}^\uparrow(i\omega_n) \hat{\Delta}_j(i\omega_n) \hat{G}_{ji}^\downarrow(i\omega_n) \right]. \quad (2)$$

Here T is the temperature, and $\hat{\Delta}$ is the onsite exchange potential giving the exchange splitting at sites i and j ; \hat{G}_{ij}^σ is the intersite Green's function projected over spin σ that can have values $\{\uparrow, \downarrow\}$ and ω_n is the n^{th} fermionic Matsubara frequency. All the terms in the above expression are matrices in orbital and spin space with the trace running over the orbital degrees of freedom. The summation is over Matsubara frequencies (ω_n). To ensure precise convergence in our analysis of exchange parameters, we increased the k -mesh to $52 \times 52 \times 26$ for these calculations. We note that the exchange interactions in this system are very similar within the non-relativistic and fully-relativistic limits (see a comparison in section II of the SM).

We employed the force theorem to determine the magnetic anisotropy, as this method has greater efficiency and accuracy from a computational point of view compared to the method based on total magnetic energies for different orientations of the global spin axis, as discussed, e.g., in previous works [48, 49]. In this approach, we first conducted non-relativistic self-consistent DFT calculations using the RSPt code. Once we obtained the converged potential and charge density, we performed three fully relativistic non-self-consistent (single-iteration) calculations with magnetic moments aligned along the three mutually orthogonal [100], [010] and [001] Cartesian directions. The magnetic anisotropy energy (MAE) was then calculated by taking the difference between the eigenvalue sums for the in-plane and out-of-plane magnetic moment directions. For the MAE calculations, we used a converged

$60 \times 60 \times 30$ k -mesh, slightly finer than for the J_{ij} calculation.

B. Atomistic Spin Dynamics Simulations

In the next step, spin textures were simulated by atomistic spin dynamics using the Uppsala Atomistic Spin Dynamics (UppASD) package [50,51], where also the inclusion of spin-lattice coupling effects can be done in a systematic first-principles way following the methodology in [52]. In this work, we focus on the spin part of the system and solve the Landau-Lifshitz-Gilbert (LLG) equation [53,54] for the atomic magnetic moments:

$$\frac{d\vec{m}_i}{dt} = -\frac{\gamma}{1+\alpha^2} \vec{m}_i \times [\vec{B}_i + \vec{b}_i(t)] - \frac{\gamma}{m_i} \frac{\alpha}{1+\alpha^2} \vec{m}_i \times (\vec{m}_i \times [\vec{B}_i + \vec{b}_i(t)]). \quad (3)$$

Here, γ is the gyromagnetic ratio and $\vec{b}_i(t)$ is a stochastic magnetic field with a Gaussian distribution. The magnitude of this field is related to the damping parameter α , which helps bring the system into thermal equilibrium, and temperature T . We use a time step of $\Delta t = 0.1$ fs for the annealing phase and $\Delta t = 1$ fs for the measurement phase in the UppASD calculations to solve these differential equations.

The effective field \vec{B}_i experienced by each spin i is derived from the partial derivative of the Hamiltonian H with respect to the local magnetic moment,

$$\vec{B}_i = -\frac{\partial H}{\partial \vec{m}_i}. \quad (4)$$

The Hamiltonian H includes all relevant interactions and is given by:

$$H = -\frac{1}{2} \sum_{i \neq j} J_{ij} \vec{e}_i \cdot \vec{e}_j - K_U \sum_i (\vec{e}_i \cdot \vec{z})^2 - \sum_i \vec{B}_{\text{ext}} \cdot \vec{e}_i, \quad (5)$$

where the first term describes the Heisenberg exchange, the second term is the uniaxial anisotropy, and the final term corresponds to the effect of an external field \vec{B}_{ext} . For small \vec{B}_{ext} , the most significant contribution to the Hamiltonian is typically from Heisenberg exchange interaction, where i and j are atomic indices, and J_{ij} is the strength of the exchange interaction, obtained from our first-principles calculations. In our atomistic spin dynamics (ASD) simulation, we used a simulation box with a size of, for example, $37 \times 37 \times 37$ containing 101,306 spins with periodic boundary conditions. We performed first a simulated annealing to bring the system into thermal equilibrium, followed by an ASD measurement phase to obtain the spin texture after the system had evolved via the LLG equation and

reached an energy minimum. The simulated annealing was done at gradually decreasing temperatures of 200 K, 100 K, 50 K, and 10 K, with 20,000 spin-dynamics sampling steps at each temperature. After these annealing steps, we performed 500,000 sampling steps during the measurement phase, so that the spin system can reach an equilibrium state at zero temperature and a given external magnetic field.

III. RESULTS AND DISCUSSION

We start with the structural details of GdRu_2Si_2 , the experimental unit cell of which [27] is shown in Fig. 1 (a). In this system, the Gd atoms are the main source of magnetism. The Gd sublattice forms a body-centred tetragonal (bct) structure as shown in Fig. 1 (b). Hence, we can see that the structure becomes quite interesting with layers of Gd atoms stacked along the \mathbf{c} -axis and separated from each other by the metallic Ru-Si networks. This initially gives an impression of a layered quasi-two-dimensional magnetic structure. However, that is far from reality, as we show in the present work. This will be evident when we discuss the magnetic properties of the system. Each Gd layer separated by the Ru-Si network discussed above forms a 2D square lattice as shown in Fig. 1 (c). The tetragonality ratio c/a of the system is such that the Gd atom at the body-centered position along the [111] direction of the unit cell becomes the second neighbor atom concerning the central atom as indicated in Fig. 1 (b). The third neighbour atom lies along the [110] in-plane direction of the square lattice as pointed out in Fig. 1 (c). The first, second, and third neighbours are shown here in the structural description as they become important in understanding the magnetic exchange and the magnetic properties.

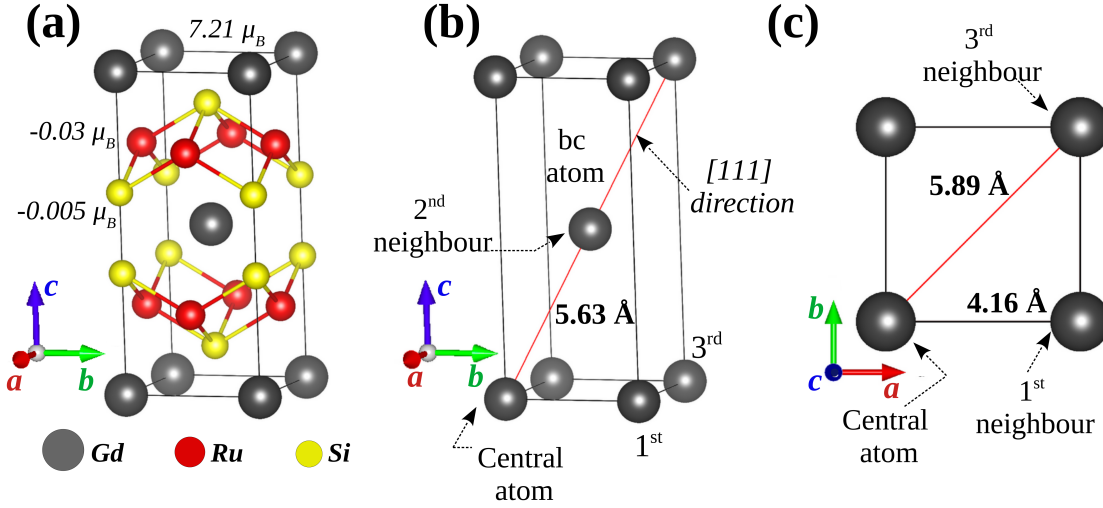


FIG. 1. (a) The experimental tetragonal unit cell of GdRu_2Si_2 with almost a layered structure. The 2D Gd layers are separated from each other by the Ru-Si networks along the c -axis. (b) Position of the Gd atoms in the unit cell showing the formation of a body-centred tetragonal sublattice. The second neighbour direction and the corresponding Gd-Gd distance are shown. (c) Square lattice arrangement of the Gd atoms in the ab -plane of a single Gd layer. The in-plane nearest neighbour and third neighbour directions and corresponding Gd-Gd distances are shown.

Next, we briefly discuss the basic electronic properties of the system. For this, we consider the unit cell shown in Fig. 1 (a) with FM ordering of the Gd spins. GGA+ U calculation was performed in VASP considering the Gd $4f$ states in the valence with the U and J values equal to 6.70, and 0.70 eV respectively [39]. The aim was to check the interaction between the $4f$ and other valence states of the system. The calculated total density of states (DOS) and atom-projected partial density of states (PDOS) are shown in Fig. 2 (a). From these plots, we can see that the system is metallic. Though we have an FM order, the exchange splitting of the states near Fermi energy (E_F) is weak. Large exchange splitting due to the FM order is only visible for the localized Gd $4f$ states (blue lines) far away from E_F . Major contributions at E_F come from the Ru $4d$ (about 65%) and Gd $5d$ (about 30%) states as shown by the red and black lines respectively. Si $3p$ states have a minimal contribution around E_F and can be ignored. These states form a pool of conduction electrons distributed within the system. To check the nature of this distribution, a small energy window of 0.20 eV was considered around the Fermi level, and the charge density (CD) corresponding

to those states was calculated as shown in Fig. 2 (b) and (c) from two different angles. An isosurface level was selected in such a way as to make the CD visible around both the Ru and Gd atoms. The charge density does not show a layered-type structure localized in the individual Gd and Ru-Si atomic layers. We can see prominent links connecting the charge densities around Gd and Ru atoms as shown in Fig. 2 (c). Most importantly, a strong intralayer contact between the Gd atoms via the CD is missing. Instead, the Gd atoms get connected indirectly via the Ru atoms. On the other hand, the conduction electrons are the main source in this system for mediating magnetic exchange between the Gd atoms, and these interactions have been suggested to be of RKKY character [2]. For that reason, the anisotropic structure of the conduction electron density is expected to impact the magnetic exchange interactions which we discuss in the next section.

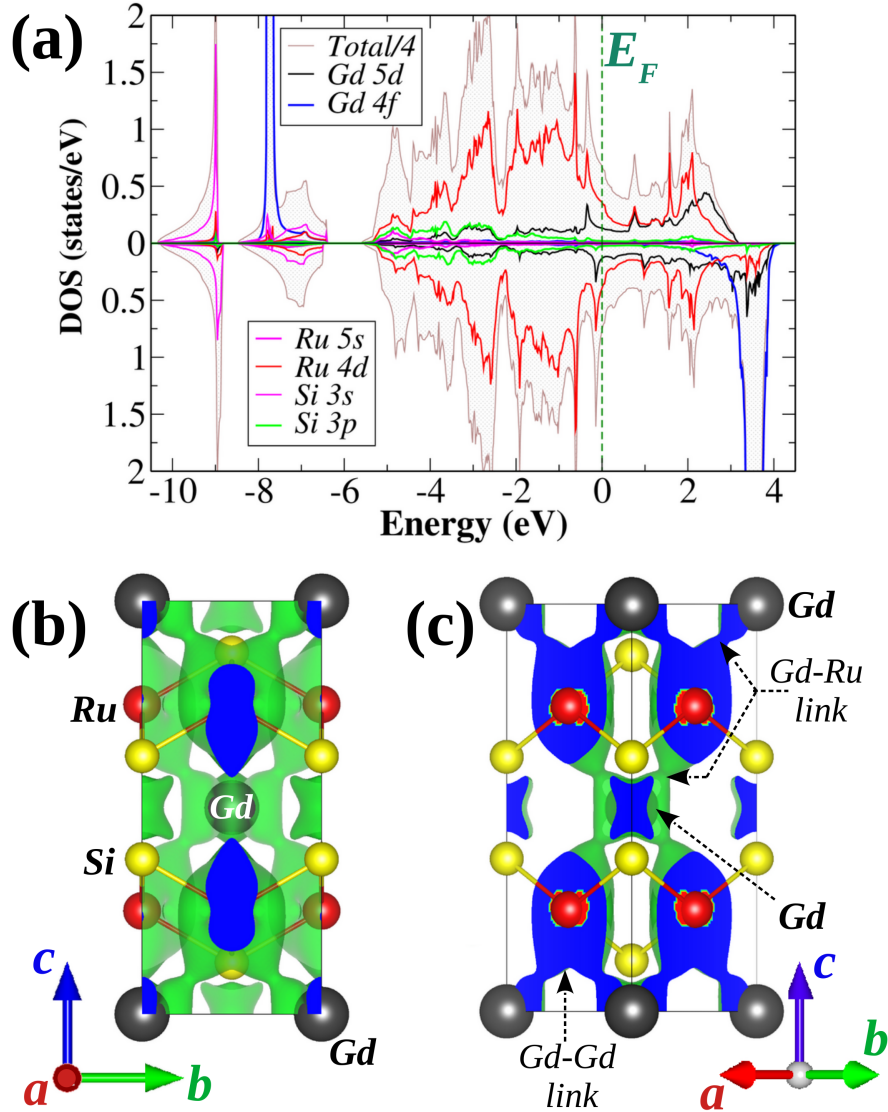


FIG. 2. (a) Total (scaled by 4) and atom+orbital projected density of states from VASP calculation where Gd 4*f* states were treated as valence states. See the main text for details. (b) and (c) shows the charge density distribution corresponding to the valence states around Fermi energy along [100] and [110] directions respectively. See the main text for more details.

In the next step, we calculated the magnetic exchange interactions for the FM reference state via magnetic force theorem (MFT) [44, 46] (review in [47]) available in the RSPt software [40–42]. The Gd 4*f* states were treated as spin-polarized core states in this calculation, since it represents non-hybridized, localized electron states, a configuration of the 4*f* states that closely represents the so called Standard Model of the rare-earths [55]. Note that a

more precise treatment would involve the so called Hubbard-I approximation, something that was investigated for the rare-earth elements in detail in Ref. [56]. However, for Gd-based systems, where the spin-up $4f$ shell is filled and spherically symmetric, a treatment of the $4f$ states as spin-polarized core or spin-polarized valence band resembles closely the Hubbard-I approximation, which motivates the approximations used here. A comparison between VASP and RSPt calculated valence electronic states around the Fermi energy E_F is shown in Fig. S1 from section I of the SM. Magnetic interactions (J_{ij}) between Gd moments at different distances (d) (scaled by the lattice constant a) are shown in Fig. 3 (a). We see a nearly alternating FM and AFM coupling with the neighbouring atoms reminiscent of a free carrier-mediated RKKY type exchange [2], a well-known mechanism in intrinsic[57] and extrinsic[58, 59] metallic magnets. RKKY has also been claimed in recent studies as the primary mechanism for magnetic interactions in this system [13, 22, 60]. To confirm this, we have separately plotted J_{ij} as a function of the interatomic distance R_{ij} along the in-plane \mathbf{a} -axis as shown in the first panel of Fig. 3 (b). Note that $J_{ij}(R_{ij})$ decays quickly making it impossible to view its oscillatory properties. To overcome this and take into account the estimated scaling factor of $1/R_{ij}^3$ for RKKY interaction in metallic 3D systems, we plot $J_{ij} \cdot R_{ij}^3$ as a function of R_{ij} as shown in the bottom panel of Fig. 3 (b). The resulting quantity $J_{ij} \cdot R_{ij}^3$ shows prominent oscillatory behaviour revealing the RKKY type exchange mechanism present in the system. Hence, long-ranged interatomic exchange with non-negligible interaction strength is not unexpected in this system as can be seen from Fig. 3 (a), where the 2nd (J_2) and 7th (J_7) interactions come out to be stronger than the 1st (J_1) and 3rd (J_3) interactions. These four interactions are important and are discussed below in more detail. The 1st, 2nd, and 3rd neighbour exchange paths are shown in Fig. 1 and have been discussed in the previous sections. The 7th neighbour exchange path is shown in the inset of Fig. 3 (a), which is along the \mathbf{c} -axis in the out-of-plane directions. To summarize, J_1 and J_3 are two intralayer exchange interactions that are weakly AFM, while J_2 and J_7 on the other hand are two interlayer interactions that are FM in nature and stronger than the intralayer interactions. A stronger interlayer exchange suggests that the system should not be treated as a layered 2D magnetic system. Interlayer exchange, if considered alone, will stabilize a FM ordering without any magnetic frustration. However, the two intralayer AFM exchange interactions on the square lattice by symmetry should lead to an exchange frustration and an overall non-collinear state is expected. This is in line with the experimental report of a

helical spiral state within the Gd layers at low temperature (T) and field (H) with an in-plane spiral modulation vector $\mathbf{Q}_{100}^{\text{Exp}} = (0.22, 0, 0)$ along the \mathbf{a} -axis in the unit of reciprocal lattice vector \mathbf{a}^* [5, 22]. As in this system the helical order mainly results from Heisenberg exchange frustration in the absence of any DMI, a Fourier transform $J(q)$ of our calculated J_{ij} 's or the adiabatic magnon spectra (AMS) can indicate the presence of such a modulation vector. This analysis, in turn, may confirm or refute the correctness of our calculated exchange interactions. In the $J(q)$ calculation, $R_{d/a}$ is a parameter defining the cut-off radii of a sphere around any magnetic site, measured in the unit of the lattice constant a . Only J_{ij} 's between that magnetic site and its neighbours inside the sphere are considered for the calculation of $J(q)$ and hence, it is expected to change with $R_{d/a}$. In Fig. 3 (c), we show $J(q)$ for $\mathbf{q} \parallel \mathbf{a}$ in the units of reciprocal lattice vector \mathbf{a}^* , for different $R_{d/a}$ values. We can see that an FM stability only occurs for $R_{d/a} = 2$ and becomes unstable for $R_{d/a} \geq 3$ where a spin-spiral state with a modulation vector \mathbf{Q}_{100} becomes favorable. $|\mathbf{Q}_{100}|$ is identified by the value of q where $J(q)$ reaches a maximum. For each considered $R_{d/a}$, the values ($|\mathbf{Q}_{100}|$, $J(|\mathbf{Q}_{100}|)$) are shown in the inset of Fig. 3 (c). \mathbf{Q}_{100} increases in magnitude gradually and becomes equal to the experimentally reported $\mathbf{Q}_{100}^{\text{Exp}}$ for $R_{d/a} = 7$. The increase in the values of ($|\mathbf{Q}_{100}|$, $J(|\mathbf{Q}_{100}|)$) beyond $R_{d/a} = 5$ is a bit unexpected and surprising, as we can see from Fig. 3 (a) that most of the calculated J_{ij} 's for $d/a \geq 5$ are significantly below the accuracy of DFT calculations and can be considered to be equal to zero. Also, as our goal is to perform ASD simulations in UppASD, considering the large number of pair interaction J_{ij} 's for $R_{d/a} = 7$ will require impractical computational resources for calculating the effective field. For $R_{d/a} = 5$, $J(q)$ predicts a spin-spiral modulation vector $(0.19, 0, 0)$ which is also close to the experimentally reported $\mathbf{Q}_{100}^{\text{Exp}}$. Furthermore, $J(q)$ and the corresponding \mathbf{Q}_{100} for $R_{d/a} = 5$ also agree well with the ones reported in a recent computational study [22] where it was possible to stabilize the SkL phase in this system by tuning the single-site anisotropy to some specific range of values. Hence, we decided to consider the exchange interactions J_{ij} up to a distance of five lattice parameters ($d/a = 5$).

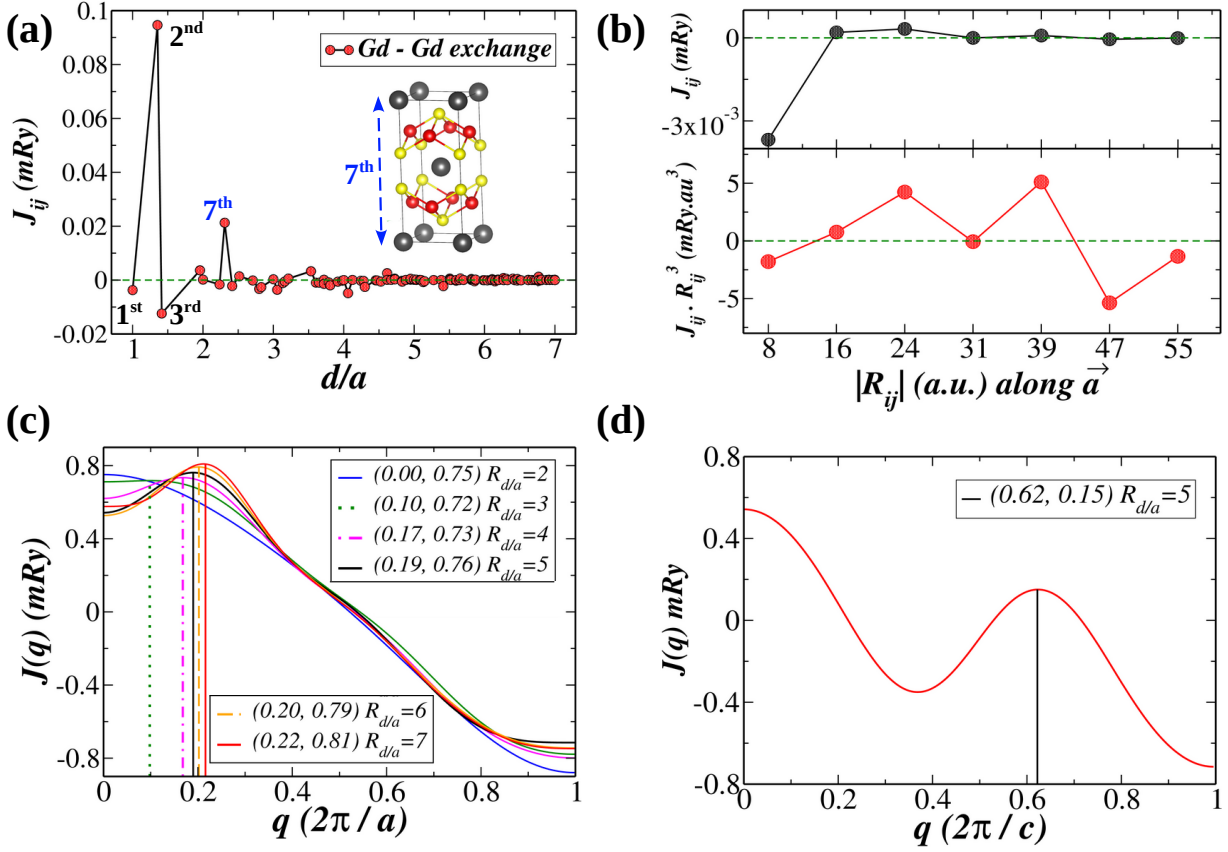


FIG. 3. (a) Calculated Gd-Gd interatomic exchange interactions as functions of distance (d) scaled by the lattice constant (a). The inset depicts the exchange path corresponding to the 7th interaction in the out-of-plane direction. (b) As functions of distance R_{ij} along the crystallographic a -axis, J_{ij} and $J_{ij} \cdot R_{ij}^3$ reveal oscillations which point at the RKKY exchange mechanism. (c) Fourier transforms $J(q)$ of the calculated exchange J_{ij} for \mathbf{q} along \mathbf{a} in the unit of $2\pi/a$ for different values of the cutoff radii $R_{d/a}$. The inset shows the (x,y) coordinates corresponding to the maxima of $J(q)$ (see the main text for details). (d) Fourier transform $J(q)$ of the calculated exchange J_{ij} for \mathbf{q} along \mathbf{c} in the unit of $2\pi/c$ with $R_{d/a} = 5$.

Now, a modulation vector of $\mathbf{Q}_{100} = (0.19, 0, 0)$ in the units of $|\mathbf{a}^*| = 2\pi/a$, suggests an in-plane periodicity or wavelength of $\lambda_{100} = 5.26a$ corresponding to the helical spiral state, which is incommensurate with the lattice periodicity. However, an integer multiple of λ_{100} , ($n \times \lambda_{100}$) could become close to ($m \times a$) and be almost lattice-commensurate for some values of n , where n and m are integers. This information is important for choosing the dimensions of the simulation cell for the ASD simulations and is provided in Table I for reference. Due to

the square lattice symmetry of the Gd layers, a helical spiral phase could result from either a modulation vector \mathbf{Q}_{100} along \mathbf{a} or \mathbf{Q}_{010} along \mathbf{b} having the same magnitude. Both of them result in analogous solutions which are energetically degenerate. According to experimental reports [5], with an external magnetic field application, the helical phase transforms into a skyrmion lattice (SkL) phase. This phase can be characterized by the simultaneous presence of a \mathbf{Q}_{100} and \mathbf{Q}_{010} with equal magnitudes [61, 62]. Hence, to incorporate these phases in the ASD calculations, a simulation cell with the in-plane dimension $m \times m$ shall be an appropriate choice, where m is an integer satisfying the condition $(n \times \lambda_{100}) \approx (m \times a)$ as closely as possible. From Table I, we can further see that any arbitrary value of m will not be able to accommodate an integer number of wavelengths of the spiral states. As a result, for the best outcome from the ASD simulation, the values of m reported in Table I, and as large as possible shall be considered for a simulation cell with in-plane dimension $m \times m$. Among these “recommended” integer m values, some of them might be preferable, based on how well the condition $(n \times \lambda_{100}) \approx (m \times a)$ is satisfied. This can be characterized by the mismatch $\frac{n\lambda_{100} - m \cdot a}{n\lambda_{100}} \times 100\%$, which is also shown in Table I for different m values. These considerations become crucial for this system as the exchange interactions are quite weak and frustrated. A larger deviation from the calculated values of m acts as a perturbation and can destabilize the spiral states.

TABLE I. Integer ($n = 1$ to 10) multiple of the theoretically obtained in-plane spiral wavelength λ_{100} and the closest simulation cell dimensions ($m \times m \times m$) that can accommodate this spin spiral. Mismatch between the cell dimensions and the spiral wavelength is shown as well, calculated as $\frac{n\lambda_{100} - m \cdot a}{n\lambda_{100}} \times 100\%$, to characterize how optimal the choice of the simulation cell is.

$Q_{100} = (0.19, 0, 0) \frac{2\pi}{a}$; $\lambda_{100} = 5.26a$			
n	$n \times \frac{\lambda_{100}}{a}$	integer 'm'	mismatch
1	5.26	5	4.9%
2	10.52	11	4.6%
3	15.78	16	1.4%
4	21.04	21	0.2%
5	26.30	26	1.1%
6	31.56	32	1.4%
7	36.82	37	0.5%
8	42.08	42	0.2%
9	47.34	47	0.7%
10	52.60	53	0.8%

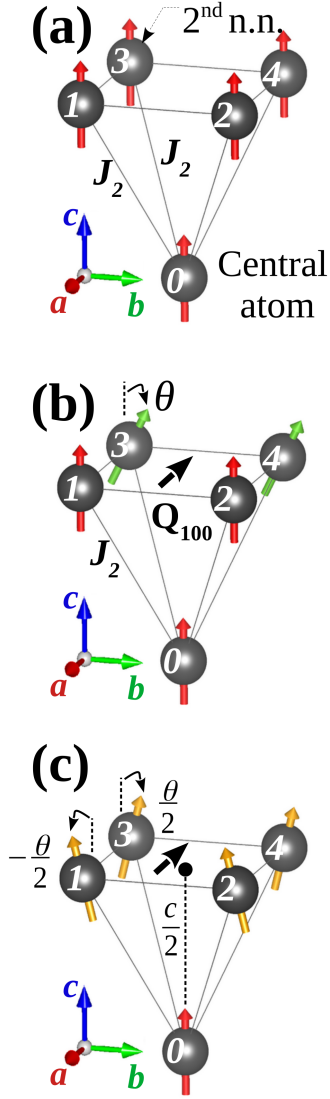


FIG. 4. (a) The central Gd atom from the unit cell origin and its four second nearest neighbours (n.n.) along the [111] directions on the top Gd layer with an FM coupling due to the exchange J_2 . (b) A phase difference θ between the four Gd spins on the top layer along a -axis in the helical phase due to the presence of the modulation vector Q_{100} . (c) The same helical phase but with a slightly different spin configuration on the top layer.

Since the experimental report [5] of an interesting and rich $B-T$ magnetic phase diagram of this system, there are several theoretical and computational efforts to understand it [13, 22, 39, 60, 63]. The two in-plane modulation vectors \mathbf{Q}_{100} and \mathbf{Q}_{010} have been considered important parameters in that respect. The obvious reason is that the spin configurations corresponding to different magnetic phases appear and have been observed within each 2D plane of the Gd square lattice. The interlayer coupling between the Gd layers has been considered as weakly FM [22] and hence is expected to play no major role in the magnetic properties. Our calculations, however, suggest that this is not true as we find the FM interlayer exchange to be the strongest magnetic interaction in the system, even stronger than the nearest-neighbor intralayer AFM couplings, which means that GdRu_2Si_2 is essentially a 3D magnet. This together with the bct sublattice of the Gd atoms makes the magnetic phases much more complex than they appear to be. To understand the interlayer interactions/coupling and its role on the magnetic properties, we have plotted the variation in $J(q)$ for $\mathbf{q} \parallel \mathbf{c}$ in the units of reciprocal lattice vector \mathbf{c}^* . This is been demonstrated in Fig. 3 (d) for $R_{d/a} = 5$. FM stability appears as expected due to a strong FM interlayer exchange. Still, a second peak of $J(q)$ is observed at $0.62\mathbf{c}^*$ suggesting, in principle, the possibility of some non-collinear spin-spin correlation between the neighbouring Gd layers along the direction of the \mathbf{c} -axis. The following discussion on the role of the strongest interlayer FM exchange J_2 in the helical state (phase-1) will help us understand the interlayer spin correlations. Fig. 4 (a) shows the central Gd atom (0^{th}) from the unit cell origin and its four 2^{nd} nearest neighbours (1 to 4) in the next Gd layer forming the square lattice. An FM ordering between the 0^{th} atom and its four 2^{nd} nearest neighbors results from ferromagnetic J_2 interaction. As a result, the four Gd spins on the top layer also appear to be FM coupled with each other as shown in the figure. This happens because the intralayer exchange has not been considered here, which should otherwise induce a helical ground state for $H = 0$. In the helical state, the four spins on the top layer in Fig. 4 (a) cannot remain in phase, because a helical state with the modulation vector \mathbf{Q}_{100} is preferred as shown in Fig. 4 (b). A phase difference of $\theta = Q_{100} \cdot a$ in the 3^{rd} and 4^{th} spins with respect to the 1^{st} and 2^{nd} spins results from the \mathbf{Q}_{100} -modulation. Due to this, it is evident that the 0^{th} spin cannot remain in phase with the four spins on the top layer simultaneously. From Fig. 4 (b) we can see that if it stays in phase with the 1^{st} and 2^{nd} spins, a phase difference of θ must occur with the 3^{rd} and 4^{th} spins. The helical state shown in Fig. 4 (b) can also be realized with a slightly different spin

configuration as depicted in Fig. 4 (c). If we ignore the 0th spin and exchange J_2 , then both Fig. 4 (b) and Fig. 4 (c) represent the same magnetic state (helical state) on the top layer and are energetically degenerate. In both cases, the phase difference between two neighbouring spins along \mathbf{a} is θ due to \mathbf{Q}_{100} . However, if we consider the interlayer interaction J_2 with the 0th spin, then the configuration in Fig. 4 (c) shall become energetically more favourable over the configuration in Fig. 4 (b). This can be seen from the energy differences between the spin configurations in Fig. 4a-c. If we consider unit spins on the Gd atoms, then the energy difference between configurations (b) and (a) is $E_b - E_a = 4J_2(1 - \cos^2(\theta/2))$, whereas for the configurations (c) and (a) $E_c - E_a = 4J_2(1 - \cos(\theta/2))$. Now, for any small value of the spin canting angle θ , $\cos^2(\theta/2) < \cos(\theta/2)$, and hence $E_c < E_b$. So the helical-state spin configuration in Fig. 4 (c) is energetically preferable.

This analysis shows an important spin correlation between the second neighbour spins along the body-diagonal direction ($\mathbf{a} + \mathbf{b} + \mathbf{c}$) or [111]. In the helical state, if we have an intralayer phase difference of θ between two neighbours along \mathbf{a} or \mathbf{b} due to \mathbf{Q}_{100} or \mathbf{Q}_{010} , then an interlayer phase difference of $\theta/2$ must occur between two neighbouring spins along ($\mathbf{a} + \mathbf{b} + \mathbf{c}$) having a distance of $|\mathbf{a} + \mathbf{b} + \mathbf{c}|/2$ between them. As a result, the phase difference between the 2nd neighbors along the ($\mathbf{a} + \mathbf{b} + \mathbf{c}$) direction with a distance of $|\mathbf{a} + \mathbf{b} + \mathbf{c}|$ between them should be θ . This data suggests that in the helical state if we have a modulation vector \mathbf{Q}_{100} along \mathbf{a} with a corresponding wavelength of λ , then there shall be another modulation vector \mathbf{Q}_{111} along ($\mathbf{a} + \mathbf{b} + \mathbf{c}$) with the same wavelength λ but in the units of ($\mathbf{a} + \mathbf{b} + \mathbf{c}$). We do find this in our ASD simulations, as well be discussed in the next section. Note that \mathbf{Q}_{111} cannot be ignored and defines the magnetic phases in GdRu₂Si₂ together with \mathbf{Q}_{100} or \mathbf{Q}_{010} . This happens due to the 3D nature of the magnetic properties of the system that must be taken into account while doing the ASD simulations. If we consider a simulation cell with the generalized dimension $N_1 \times N_2 \times N_3$, then the presence of \mathbf{Q}_{100} or \mathbf{Q}_{010} in the helical phase and both of them in the SkL phase requires (i) $N_1 = N_2 = m$ so that the simulation cell is compatible with the wavelength of the magnetic phase, where m is one of the integer values from Table I. However, the presence of \mathbf{Q}_{111} along with \mathbf{Q}_{100} and \mathbf{Q}_{010} requires (ii) $N_1 = N_2 = N_3 = m$. Deviating from these conditions shall result in additional perturbation in the spin system and is expected to destabilize the spin states. To check if our reasoning is correct, we performed ASD simulations with three different simulation cells having dimensions $37 \times 37 \times 37$, $37 \times 37 \times 21$, and $37 \times 37 \times 3$ respectively at $H = 0$ and $T = 0$.

Note that in these simulations we modify only one dimension of the simulation cell, while the rest of the computational parameters and the spin Hamiltonian remain the same. The first cell should produce the expected helical phase as reported in previous experiments. In contrast, the second and third calculation is expected to show additional spin distortions as we deviate from the $N_1 = N_2 = N_3 = m$ condition. In the second calculation, we violate the $N_1 = N_2 = N_3 = m$ condition by choosing $N_3 = 21$, which is also a good number from Table I to accommodate an integer number of spiral wavelengths. In the third calculation, we do this by setting $N_3 = 3$, which is less than 5, the minimum value required to accommodate a single wavelength. In this case, we expect major frustration and destabilization of the helical spiral phase. In these ASD simulations, only the exchange interactions (J_{ij}) and uniaxial anisotropy energy (K_U) of ~ 0.05 meV along the out-of-plane \mathbf{c} -axis were considered in the spin Hamiltonian (Eqn. 5). K_U was calculated from DFT following a method described in detail in the methodology section. The value is in agreement with the one reported in recent literature [39].

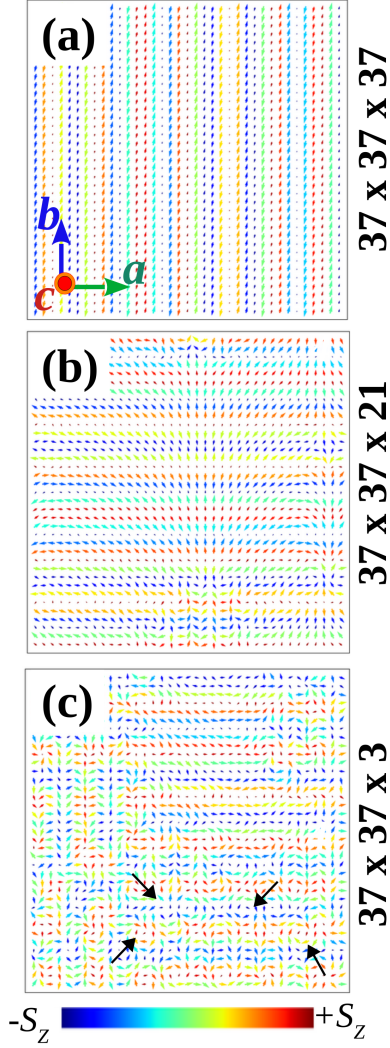


FIG. 5. Spin configuration after ASD simulations, on the top Gd layer of the simulation cell with dimension (a) $37 \times 37 \times 37$, (b) $37 \times 37 \times 21$, and (c) $37 \times 37 \times 3$ respectively.

The spin configuration on the topmost Gd layer of the simulation cell from the three calculations is presented in Fig. 5. The simulation cell with the dimension $37 \times 37 \times 37$ correctly produces the helical phase with a \mathbf{Q}_{100} as shown in Fig. 5 (a). The $37 \times 37 \times 21$ still produces a helical state defined by a \mathbf{Q}_{010} but with additional distortions as shown in Fig. 5 (b). The $37 \times 37 \times 3$ simulation cell cannot reproduce the helical state as depicted in Fig. 5 (c). Instead, we observe a spin state with some isolated skyrmion-like spin vortices, that are marked by small black arrows. This result is interesting as it opens up for a new avenue to stabilize a skyrmion configuration, outside of the common approach of applying an external magnetic field. Hence this observation could be exploited to stabilize skyrmion

textures in magnetic files, including the skyrmion lattice.

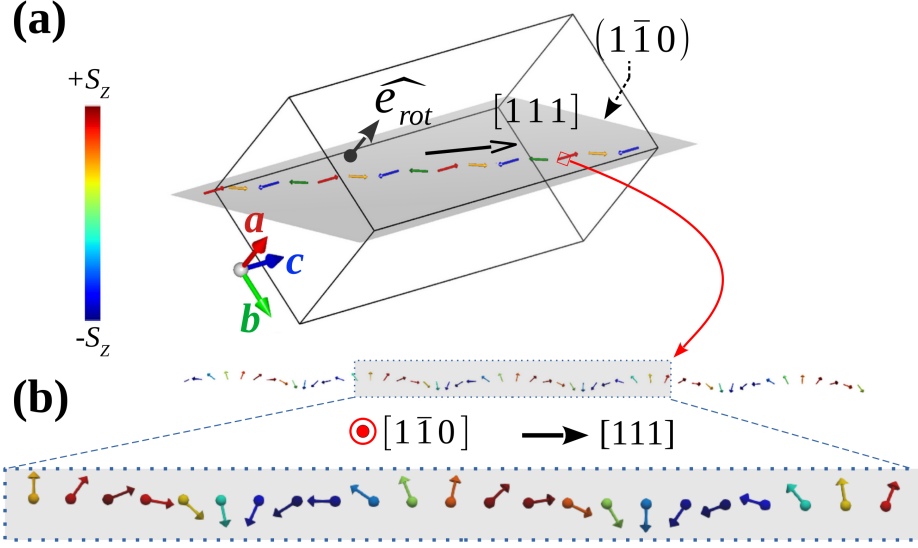


FIG. 6. (a) The presence of a spin-spiral in the atomic chain along the $[111]$ direction in the ground state where the spins in the 2D (001) planes form a helical spiral along the $[100]$ direction (see Fig. 5 (a)). (b) Cycloidal nature of the interlayer spiral along $[111]$ with a spiral rotation vector along $[1\bar{1}0]$.

Finally, in Fig. 6 we show the arrangements of the spins in the atomic chain along the $(\mathbf{a} + \mathbf{b} + \mathbf{c})$ or $[111]$ direction in the proper helical phase coming from the $37 \times 37 \times 37$ cell simulation shown in Fig. 5 (a). The spin arrangements clearly show a cycloidal type spin-spiral as shown in Fig. 6 (b) propagating along the $[111]$ direction confirming the presence of the \mathbf{Q}_{111} modulation vector. In this cycloidal spiral, the spins mainly lie on the $(1\bar{1}0)$ plane and rotate about to the spiral rotation direction \hat{e}_{rot} nearly parallel to the $[1\bar{1}0]$ direction as shown schematically in Fig. 6 (a).

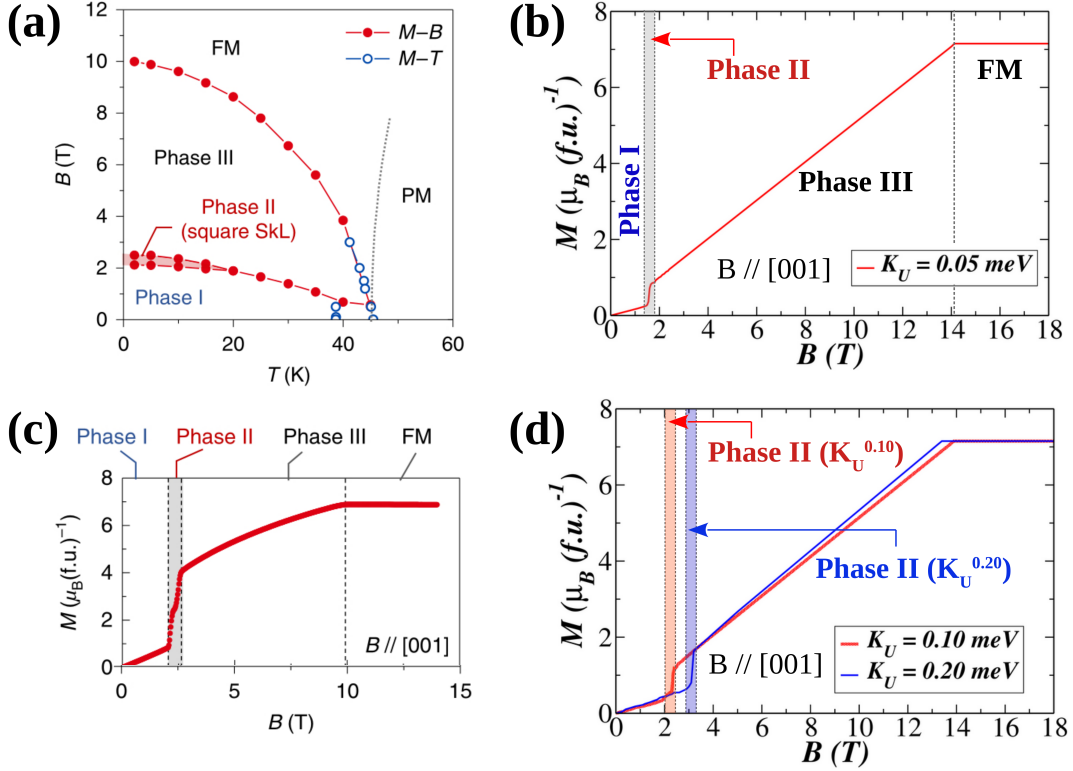


FIG. 7. LEFT PANEL: The experimentally reported (a) $B - T$ phase diagram of GdRu₂Si₂ and (c) the corresponding M vs B variation at $T = 5$ K. Plots (a) and (c) are taken from experimental work [5] to compare with our calculated data. RIGHT PANEL: (b) Theoretically calculated M vs B data for $K_U = 0.05$ meV, showing the presence of three different phases before the FM phase similar to the experimental report. (d) $M(B)$ curves for two different anisotropy constants; these results indicate a somewhat better quantitative agreement with experiment for a slightly increased value of K_U .

Having understood the role of interlayer coupling and the importance of the interlayer modulation vector \mathbf{Q}_{111} , we can expect that an ASD simulation taking into account the presence of both \mathbf{Q}_{100} and \mathbf{Q}_{111} along with a Zeeman term in the spin Hamiltonian (Eqn. 5) shall be able to reproduce the experimentally reported $B - T$ phase diagram [5] as shown in Fig. 7 (a). This phase diagram was generated in [5] by identifying the magnetic field values (B) where a magnetic phase transition was observed in the M vs B measurements as shown in Fig. 7 (c) for $T = 5$ K. Such measurements were performed for different T values to get the full $B - T$ phase diagram. Hence, everything boils down to calculating the

M as a function of B for different temperatures. The low-temperature region of the phase diagram in Fig. 7 (a) suggests that the experimental M vs B measurements for $T = 5$ K and 0 K shall be almost identical. Based on this observation, we decided to perform ASD simulations for a range of external field values at zero temperature to get $M(B)$ curves (example in Fig. 7 (c)) and compare them with the experimental data. We get a good qualitative agreement showing the presence of three distinct phases before entering the fully polarized FM phase, similarly to experiment. However, there is a noticeable quantitative deviation from the experimental data. For example, our data shows the transition to the FM state at $B \sim 14$ T, whereas in experiment it is found at ~ 10 T. Experimental data shows the occurrence of Phase II for magnetic field values between $B = 2.0$ T and 2.3 T, whereas in our calculation it appears between $B = 1.6$ T and 1.9 T. Also, the variation of the total magnetic moment per unit cell by $\sim 1.0 \mu_B$ in Phase II is much smaller compared to the experimentally observed $\sim 3.0 \mu_B$ variation. These differences could arise from some deficiency in our spin dynamics simulations, e.g. numerical accuracy or the validity of the spin Hamiltonian. To identify that, we had a closer look at the magnetic ordering in the three phases. The spin configuration within a 2D Gd plane is presented in Fig. 8.

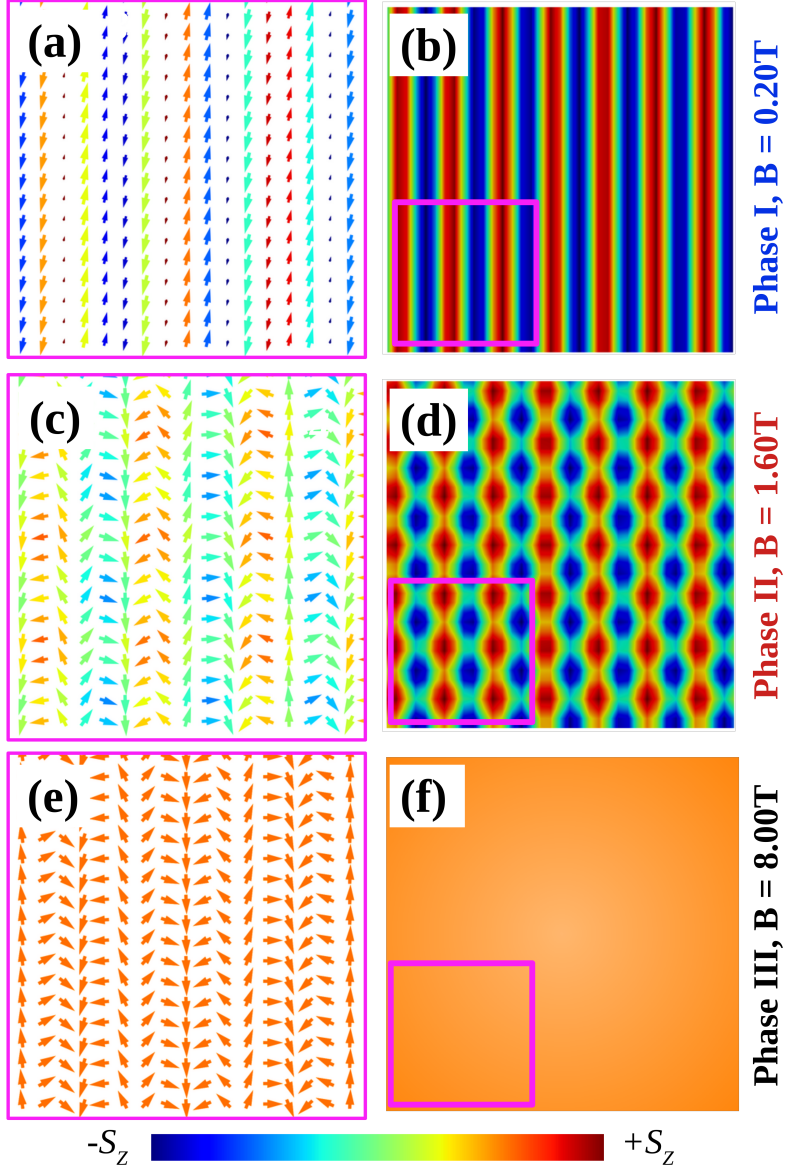


FIG. 8. LEFT COLUMN: Spin configuration within the 2D Gd layers in (a) Phase I, (c) Phase II, and (e) Phase III, respectively, after the ASD simulation with $K_U = 0.05$ meV, same as in Fig. 7 (b). The SkL state observed experimentally is not stabilized in Phase II. RIGHT COLUMN: S_z component of a spin-density function replacing the individual spins within the 2D Gd layers in (b) Phase I, (d) Phase II, and (f) Phase III respectively. In Phase II we get a square lattice distribution of $+S_z$ and $-S_z$ densities similar to the SkL state but the in-plane components of the spins fail to generate the skyrmions.

We get the reported screw spiral or helical spiral corresponding to Phase I, and the fan type or the conical spiral in Phase III. These spin orderings in a single Gd layer from the top of the simulation cell are shown in Fig. 8 (a) and (e), respectively. We can also identify these two phases with the \mathbf{Q} vectors in the calculated spin structure factor which are not reported here in the main text but are included in section III of the SM. In Phase I, we see a single \mathbf{Q}_{100} modulation of both the in-plane ($S_x + S_y$) and out-of-plane (S_z) spin component as expected. In Phase III, the \mathbf{Q}_{100} modulation of S_z is absent and we see a FM ordering instead, which is again a signature of the conical spiral. Now we focus on Phase II (Fig. 8 (c)) which is not the expected SkL phase observed experimentally in [5]. This phase is also neither Phase I nor Phase III but something different which becomes more evident when we try to compare the real space spin-density distribution of the z -component of the spin density (Fig. 8 (b), (d), and (f)). In Phase II we see a unique square lattice distribution of spin-up and spin-down densities in a checkerboard manner which cannot be found in Phase I and III. Interestingly, this square-lattice distribution of S_z density is something to expect also in the measured SkL phase. This happens due to a double- \mathbf{Q} ($\mathbf{Q}_{100} + \mathbf{Q}_{010}$) modulation of S_z that we can see from the spin structure factor in Fig. S3 of the SM, again very similar to what happens in the SkL phase. However, a similar double- \mathbf{Q} modulation of ($S_x + S_y$) expected for that SkL state [63] is missing in our simulated Phase II, and this fact prevents the SkL from appearing fully. Hence, the quantitative deviation of the simulated M vs B data (Fig. 7 (b)) from the experimentally measured curves (Fig. 7 (c)) can be considered as a sign of a more major problem, the unknown deficiencies or inaccuracies in our ASD simulations destabilizing the SkL state in Phase II. Our simulations so far give a good qualitative description of the magnetic response which suggests the absence of numerical inaccuracies. Hence, we could safely ascribe the aforementioned problem to the deficiencies of the spin Hamiltonian that we use. There are three main reasons to believe this which we will now discuss in detail. Each of them requires to be investigated separately and together to improve the spin Hamiltonian and make it closer to the physical reality for this system. At the same time, the considerations shown below can be important for many other magnets with topological or non-collinear orders.

First, we want to discuss the role of uniaxial anisotropy and the value $K_U \sim 0.05$ meV that we obtain from DFT calculations and use in our simulations. K_U is one of the intrinsic magnetic parameters present in our spin Hamiltonian along with the isotropic exchange in-

teractions for ASD simulations. Recent computational study by Bouaziz *et al.* [22] reports the stabilization of the SkL phase in this system using a spin Hamiltonian similar to what we have considered. According to that study, a double- \mathbf{Q} square SkL arises from the combination of crystal symmetry-dependent frustrated RKKY interactions with a simple uniaxial magnetocrystalline anisotropy (K_U) and a magnetic field perpendicular to the helical axis. However, to achieve this, K_U was required to be tuned around 0.30 meV. A value of 0.05 meV that we are using in our simulations was found to be insufficient for the SkL phase. There are also a few interesting points to notice in the reported $B - K_U$ phase diagram. It shows the SkL phase to occur around an external magnetic field of $B = 1.0$ T for K_U around 0.30 meV which is half the experimentally reported value of $B = 2.0$ T. Additionally, the phase diagram shows the transition to the FM phase directly avoiding Phase III, when the external field B was increased. This is in contradiction with the experimental phase diagram and our data that both suggest the highest stability of Phase III compared to Phase I and Phase II in a certain range of applied magnetic field. Getting inspired by these previously reported results of SkL phase stabilization for $K_U = 0.3$ meV, we decided to increase our K_U value and recalculate the M vs B phase diagram in anticipation of getting a SkL in Phase II. This is presented in Fig. 7 (d) for $K_U = 0.1$ meV and 0.2 meV. The rest of the computational settings remained the same as for the $K_U = 0.05$ meV case. With an increased value of K_U , we see a much better quantitative agreement with the experiment as Phase II appears at higher B values of around 2.0 T showing the important role of a perpendicular uniaxial anisotropy in the stabilization of the helical spiral phase (Phase I). We also see a larger variation of M with B in Phase II compared to the $K_U = 0.05$ meV case. Most importantly, we now see the presence of isolated skyrmion-like vortices in Phase II which is in line with what was reported [22], though a proper SkL state is still missing (for a detailed discussion see section IV of the SM). These results show the possibility of achieving more skyrmions or even a SkL in Phase II by further increasing K_U to about 0.30 meV as was used in the previous work [22] for the SkL stability. But from the trend that we see in Fig. 7 (d) as a function of K_U , it is clear that for $K_U = 0.3$ meV, Phase II is going to appear for an B value of nearly 4.0 T, which is twice the experimentally reported value. However, the previous work reports a corresponding value of 1.0 T which is in disagreement with what we get. A larger value of K_U used in that work [22] also disagrees with the computed value of 0.05 meV [39]. In GdRu_2Si_2 , Gd^{3+} cations with $S = 7/2$ and $L = 0$ are expected to show

a very small or zero value of K_U due to the zero orbital moment L in this case [64]. The dimensions of the simulation cell used in [22] for ASD simulations was $60 \times 60 \times 10$, which violates the condition $N_1 = N_2 = N_3 = m$ that we propose to be essential for accurate ASD simulations for this kind of system. We have already shown in the previous section (Fig. 5 (c)), that deviating from this condition acts as an additional perturbation and could induce skyrmions even at $B = 0$ T. Hence, a simulation cell with the dimensions $60 \times 60 \times 10$ along with K_U around 0.30 meV could stabilize a SkL state as was claimed [22]. This could be exploited for a better understanding of the SkL phase and its application, but is not the purpose of our present study. We want to conclude here from our calculations that an out-of-plane anisotropy constant K_U is essential for the stability of the helical spiral ground state (Phase I). Increasing the value of K_U shall enhance the stability of the helical phase and could further stabilize isolated skyrmions in Phase II. This could be used as a tuning parameter for a better description of the phase transitions. However increasing it beyond some critical value could destabilize Phase III causing a qualitative disagreement with the experiment [5]. Hence, the uniaxial anisotropy cannot be a sufficient condition and the only driving mechanism for a field-induced SkL stability in this system.

Secondly, we want to discuss the possibility of small inaccuracies in our calculated exchange interactions J_{ij} 's which could be an important reason for the destabilization of the SkL phase. Our data so far suggests that the main source of non-collinearity in this system is the competition between the interlayer and intralayer exchange interactions. This along with an out-of-plane uniaxial anisotropy (K_U) stabilizes a helical spiral ground state in the absence of external magnetic field B . All methodologies used to calculate exchange interactions are connected to inaccuracies, and it is possible that the method used here needs to be improved in order to accurately describe the competition between different magnetic interactions in GdRu_2Si_2 . Such modifications of the exchange could lead to a spiral state deviating slightly from a perfect helix. This is in fact what we observe in our case where the spins are slightly inclined along the spiral propagation direction. This could hinder the occurrence of a Bloch-type SkL phase where a double- \mathbf{Q} helical modulation of the spins along the two orthogonal directions of a square lattice takes place [61, 62]. One indication is already there from our calculated modulation vector \mathbf{Q}_{100} determined from the Fourier transform $J(\mathbf{q})$ of the exchange parameters. To match the experimentally reported value of $(0.22, 0.0, 0.0)\mathbf{a}^*$, it is required to set $R_{d/a} = 7$, which also significantly increases the

computational effort due to the large number of spins interacting within this distance. This was unexpected as most of the calculated J_{ij} 's beyond $R_{d/a} = 5$ are close to zero and are numerically difficult to calculate accurately (see Fig. 3 (a) for details). Considering the most significant J_{ij} 's within the cutoff radius $R_{d/a} = 5$ for a Fourier transform resulted in $\mathbf{Q}_{100} = (0.19, 0.0, 0.0)\mathbf{a}^*$ that deviates slightly from the experimental value. Hence, this demands a separate investigation of how important this deviation is for reproducing the skyrmionic phase, something which is outside the scope of the present investigation. For a future study, it would be also interesting to study how sensitive magnetic interactions are to the structural details, e.g. the a - and c -lattice parameters, Si-Si interlayer separation and many other bond lengths. This can lead to changes in the spin spiral wavevector \mathbf{Q}_{100} and could affect the skyrmion stability. These studies will further reveal whether a more accurate description of, for example, the interlayer exchange is crucial for the stabilization of the SkL phase. The aforementioned planned investigations will be part of an upcoming work along with the role of weak interactions that we finally discuss in the following paragraph.

Thirdly and finally, we want to discuss the role of weak magnetic interactions not considered in our spin Hamiltonian. The microscopic magnetic interactions that we considered so far are the isotropic Heisenberg exchange (bilinear) and uniaxial anisotropy that we discussed in the previous paragraphs. These two interactions could stabilize the helical and conical states under an external magnetic field but might not be enough for the SkL phase appearing within a very narrow region of the $B - T$ phase diagram. For a symmetric tetragonal crystal like this, the importance of four-spin (biquadratic) interaction mediated by itinerant electrons in the presence of an easy axis anisotropy to stabilize a multiple- \mathbf{Q} SkL state over a single- \mathbf{Q} spiral state has been claimed before [5, 63]. The theoretical work by Hayami *et al.* [63] considers a model Hamiltonian based on a Kondo lattice model consisting of itinerant electrons and localized spins. That Hamiltonian included both bilinear and biquadratic interaction and its role was analyzed for a 2D square lattice. The biquadratic exchange interaction was found to be important in stabilizing any spin state with a double- \mathbf{Q} modulation which could be even further stabilized by bond-dependent anisotropic interactions. Such states could transform into a proper SkL state with the application of an external magnetic field. Including these weak interactions in our spin Hamiltonian could solve the problem of the missing SkL phase and even produce a better phase diagram. This further motivates us to investigate the role of other weak interactions like the magnetic dipolar and symmetric

anisotropic exchange (SAE) interactions. Magnetic dipolar interactions are naturally present in any magnetic material and could become important in a system like GdRu_2Si_2 , where large atomic moments of $7.0 \mu_B$ are present, potentially leading to non-negligible dipolar interactions. The role of dipolar exchange in stabilizing topological magnetic structures like magnetic bubbles or skyrmions is well known from previous studies for similar systems [65–67]. Our initial data from a set of simulations with dipolar exchange does indeed show more pronounced rotations of the in-plane spin components that could stabilize a SkL (data not shown here). Similarly, unlike antisymmetric anisotropic exchange (DMI interaction), the symmetric anisotropic exchange (SAE) interactions are not zero in this system, as our calculations suggest, and could act as an additional source of anisotropy. SAE-induced hexagonal skyrmion lattice (SkX) in the centrosymmetric NiI_2 monolayer without DMI was also recently reported [68]. These reports demand a thorough investigation of the role of these three weak interactions in GdRu_2Si_2 and will be discussed in depth in our follow-up work which will address the stabilization of a SkL phase in this system.

IV. CONCLUSION

GdRu_2Si_2 is a metallic magnet with Gd $4f$ moments interacting via the RKKY exchange mechanism. This triggers an exchange frustration in the system leading to non-collinearity even without any DMI. The main source of exchange frustration is the competition between interlayer and intralayer exchange, which are dominantly FM and AFM in nature respectively. Interestingly the interlayer FM exchange is much stronger compared to the intralayer AFM interactions suggesting it is a 3D bulk magnet despite its layered-type appearance. With further analysis of the exchange data, we can identify the presence of an interlayer modulation vector \mathbf{Q}_{111} which coexists with the modulation vectors \mathbf{Q}_{100} and \mathbf{Q}_{010} , known from literature. We could confirm the \mathbf{Q}_{111} -modulation of the spin texture from our spin-dynamics simulations and show that it is in line with its magnetic properties. This interlayer modulation vector cannot be ignored and describes the magnetic phases together with the experimentally observed intralayer modulation vectors \mathbf{Q}_{100} and \mathbf{Q}_{010} .

Our findings suggest that the magnetic phases in GdRu_2Si_2 are far more complex than they appear where both intralayer and interlayer spin correlation results in a complex modulation of the spins. By taking these correlations into account, our spin dynamics simulations

can reproduce the magnetic field-induced phase transitions which are in a good qualitative agreement with the experimental data. This confirms that isotropic exchange and uniaxial anisotropy are the most important interactions in this system that could explain the major magnetic properties and the phase diagram. However, our simulations are not able to stabilize the SkL phase in between the helical and conical phases in the phase diagram. This happens due to the missing double- \mathbf{Q} modulation of the in-plane components of the spins compared to the out-of-plane components where the double- \mathbf{Q} modulation exists similar to the SkL phase. We consider it as a partial stabilization of the SkL phase and ascribe it to weak additional magnetic interactions absent in our spin model.

Regarding the computational methodology, we point out the importance of supercell dimensions for modelling the magnetic state using atomistic spin dynamics. Quite different results can be obtained depending on the dimensions, even along the c -axis, relative to the wavelength of the spin spirals and sizes of the skyrmions. This can explain the difference between some of our results and previous studies. This observation can be important for spin dynamics studies of magnetic systems in general, and for non-collinear magnets in particular, where the size effects in terms of the simulation cell dimensions can be of high importance, especially when magnetic textures are not commensurate with the crystal lattice. This also carries over to the experimental investigations where thin film growth and/or nanopatterning could be used to induce and manipulate specific skyrmionic states. Further studies and experiments in this direction would potentially provide new breakthroughs and move the field of topological magnetism into the field of meta-materials, opening new vistas of this class of materials with the establishment of meta-skyrmionics.

V. ACKNOWLEDGMENTS

This work was financially supported by the Knut and Alice Wallenberg Foundation through grant numbers 2018.0060, 2021.0246, and 2022.0108 (PI's: O.E. and A.D.), and R.P. and V.B. acknowledge support from the Göran Gustafsson Foundation (recipient of the “small prize”: V.B.). O.E. and A.D. acknowledge support from the Wallenberg Initiative Materials Science for Sustainability (WISE) funded by the Knut and Alice Wallenberg Foundation (KAW). A.D. also acknowledges financial support from the Swedish Research Council (Vetenskapsrådet, VR), Grant No. 2016-05980 and Grant No. 2019-05304. O.E. also

acknowledges support by the Swedish Research Council (VR), the Foundation for Strategic Research (SSF), the Swedish Energy Agency (Energimyndigheten), the European Research Council (854843-FASTCORR), eSSENCE and STandUP. S.S. acknowledges funding (post-doctoral stipend) from the Carl Tryggers Foundation (grant number CTS 22:2013, PI: V.B.).

The computations/data handling were enabled by resources provided by the Swedish National Infrastructure for Computing (SNIC) at the National Supercomputing Centre (NSC, Tetralith cluster) partially funded by the Swedish Research Council through grant agreement no. 2018-05973 and by the National Academic Infrastructure for Supercomputing in Sweden (NAISS) at the National Supercomputing Centre (NSC, Tetralith cluster) partially funded by the Swedish Research Council through grant agreement no. 2022-06725. Structural sketches in Figs. 1–4 were produced using the VESTA3 software [69]. Spin configurations in Figs. 5 and 8 were plotted using the SpinView software [70].

We thank Saikat Sarkar (CRIS, India) and Arnob Mukherjee (UU, Sweden) for useful discussions on this study, Nastaran Salehi and Philipp Rybakov for discussions about the dipolar exchange and verification of its implementation in the UppASD software, Manuel Pereiro and Qichen Xu for similar discussions too and Anders Bergman for general discussions about the UppASD software.

-
- [1] Ślaski, M., Szytuła, A., Leciejewicz, J. & Zygmunt, A. Magnetic properties of $RE Ru_2 Si_2$ ($RE = Pr, Nd, Gd, Tb, Dy, Er$) intermetallics. *Journal of magnetism and magnetic materials* **46**, 114–122 (1984).
- [2] Ruderman, M. A. & Kittel, C. Indirect exchange coupling of nuclear magnetic moments by conduction electrons. *Physical Review* **96**, 99 (1954).
- [3] Dzyaloshinsky, I. A thermodynamic theory of “weak” ferromagnetism of antiferromagnetics. *Journal of Physics and Chemistry of Solids* **4**, 241–255 (1958). URL <https://www.sciencedirect.com/science/article/pii/0022369758900763>.
- [4] Moriya, T. Anisotropic superexchange interaction and weak ferromagnetism. *Phys. Rev.* **120**, 91–98 (1960). URL <https://link.aps.org/doi/10.1103/PhysRev.120.91>.
- [5] Khanh, N. D. *et al.* Nanometric square skyrmion lattice in a centrosymmetric tetragonal magnet. *Nature Nanotechnology* **15**, 444–449 (2020).

- [6] Fert, A., Reyren, N. & Cros, V. Magnetic skyrmions: advances in physics and potential applications. *Nature Reviews Materials* **2**, 1–15 (2017).
- [7] Seki, S. *et al.* Propagation dynamics of spin excitations along skyrmion strings. *Nature communications* **11**, 256 (2020).
- [8] Neubauer, A. *et al.* Topological hall effect in the *a* phase of mnsi. *Phys. Rev. Lett.* **102**, 186602 (2009). URL <https://link.aps.org/doi/10.1103/PhysRevLett.102.186602>.
- [9] Kanazawa, N. *et al.* Large topological hall effect in a short-period helimagnet mnge. *Phys. Rev. Lett.* **106**, 156603 (2011). URL <https://link.aps.org/doi/10.1103/PhysRevLett.106.156603>.
- [10] Shiomi, Y., Kanazawa, N., Shibata, K., Onose, Y. & Tokura, Y. Topological nernst effect in a three-dimensional skyrmion-lattice phase. *Phys. Rev. B* **88**, 064409 (2013). URL <https://link.aps.org/doi/10.1103/PhysRevB.88.064409>.
- [11] Mizuta, Y. P. & Ishii, F. Large anomalous nernst effect in a skyrmion crystal. *Scientific reports* **6**, 28076 (2016).
- [12] Fert, A., Cros, V. & Sampaio, J. Skyrmions on the track. *Nature nanotechnology* **8**, 152–156 (2013).
- [13] Nomoto, T., Koretsune, T. & Arita, R. Formation mechanism of the helical *q* structure in Gd-based skyrmion materials. *Physical review letters* **125**, 117204 (2020).
- [14] Ishikawa, e. Y., Tajima, K., Bloch, D. & Roth, M. Helical spin structure in manganese silicide MnSi. *Solid State Communications* **19**, 525–528 (1976).
- [15] Mühlbauer, S. *et al.* Skyrmion lattice in a chiral magnet. *Science* **323**, 915–919 (2009).
- [16] Lebech, B., Bernhard, J. & Freltoft, T. Magnetic structures of cubic FeGe studied by small-angle neutron scattering. *Journal of Physics: Condensed Matter* **1**, 6105 (1989).
- [17] Yu, X. *et al.* Near room-temperature formation of a skyrmion crystal in thin-films of the helimagnet FeGe. *Nature materials* **10**, 106–109 (2011).
- [18] Adams, T. *et al.* Long-wavelength helimagnetic order and skyrmion lattice phase in Cu₂OSeO₃. *Physical review letters* **108**, 237204 (2012).
- [19] Seki, S., Yu, X., Ishiwata, S. & Tokura, Y. Observation of skyrmions in a multiferroic material. *Science* **336**, 198–201 (2012).
- [20] Mühlbauer, S. *et al.* Skyrmion lattice in a chiral magnet. *Science* **323**, 915–919 (2009).
- [21] Yu, X. *et al.* Real-space observation of a two-dimensional skyrmion crystal. *Nature* **465**,

- 901–904 (2010).
- [22] Bouaziz, J., Mendive-Tapia, E., Blügel, S. & Staunton, J. B. Fermi-surface origin of skyrmion lattices in centrosymmetric rare-earth intermetallics. *Physical review letters* **128**, 157206 (2022).
- [23] Hayami, S. & Motome, Y. Topological spin crystals by itinerant frustration. *Journal of Physics: Condensed Matter* **33**, 443001 (2021).
- [24] Torikachvili, M. S., Bud’ko, S. L., Ni, N. & Canfield, P. C. Pressure induced superconductivity in CaFe_2As_2 . *Phys. Rev. Lett.* **101**, 057006 (2008). URL <https://link.aps.org/doi/10.1103/PhysRevLett.101.057006>.
- [25] Windsor, Y. W. *et al.* Exchange scaling of ultrafast angular momentum transfer in 4f antiferromagnets. *Nature Materials* **21**, 514–517 (2022). URL <https://doi.org/10.1038/s41563-022-01206-4>.
- [26] Hoffmann, R. & Zheng, C. Making and breaking bonds in the solid state: The ThCr_2Si_2 structure. *The Journal of Physical Chemistry* **89**, 4175–4181 (1985). URL <https://doi.org/10.1021/j100266a007>.
- [27] Hiebl, K., Horvath, C., Rogl, P. & Sienko, M. Magnetic properties and structural chemistry of ternary silicides (re, th, u) Ru_2Si_2 (re= rare earth). *Journal of magnetism and magnetic materials* **37**, 287–296 (1983).
- [28] Blöchl, P. E. Projector augmented-wave method. *Phys. Rev. B* **50**, 17953–17979 (1994). URL <https://link.aps.org/doi/10.1103/PhysRevB.50.17953>.
- [29] Kresse, G. & Joubert, D. From ultrasoft pseudopotentials to the projector augmented-wave method. *Phys. Rev. B* **59**, 1758–1775 (1999). URL <https://link.aps.org/doi/10.1103/PhysRevB.59.1758>.
- [30] Kresse, G. & Hafner, J. Ab initio molecular dynamics for liquid metals. *Phys. Rev. B* **47**, 558–561 (1993). URL <https://link.aps.org/doi/10.1103/PhysRevB.47.558>.
- [31] Kresse, G. & Hafner, J. Ab initio molecular-dynamics simulation of the liquid-metal–amorphous-semiconductor transition in germanium. *Phys. Rev. B* **49**, 14251–14269 (1994). URL <https://link.aps.org/doi/10.1103/PhysRevB.49.14251>.
- [32] Kresse, G. & Furthmüller, J. Efficient iterative schemes for ab initio total-energy calculations using a plane-wave basis set. *Phys. Rev. B* **54**, 11169–11186 (1996). URL <https://link.aps.org/doi/10.1103/PhysRevB.54.11169>.

- [33] Kresse, G. & Furthmüller, J. Efficiency of ab-initio total energy calculations for metals and semiconductors using a plane-wave basis set. *Computational Materials Science* **6**, 15–50 (1996). URL <https://www.sciencedirect.com/science/article/pii/0927025696000080>.
- [34] Perdew, J. P., Burke, K. & Ernzerhof, M. Generalized gradient approximation made simple. *Phys. Rev. Lett.* **77**, 3865–3868 (1996). URL <https://link.aps.org/doi/10.1103/PhysRevLett.77.3865>.
- [35] Perdew, J. P., Burke, K. & Ernzerhof, M. Generalized gradient approximation made simple [phys. rev. lett. 77, 3865 (1996)]. *Phys. Rev. Lett.* **78**, 1396–1396 (1997). URL <https://link.aps.org/doi/10.1103/PhysRevLett.78.1396>.
- [36] Anisimov, A. N. *et al.* The temperature-dependent in- and out-of-plane magnetic anisotropies in superlattices. *Journal of Physics: Condensed Matter* **9**, 10581–10593 (1997). URL <https://doi.org/10.1088/0953-8984/9/48/004>.
- [37] Kotliar, G. *et al.* Electronic structure calculations with dynamical mean-field theory. *Rev. Mod. Phys.* **78**, 865–951 (2006). URL <https://link.aps.org/doi/10.1103/RevModPhys.78.865>.
- [38] Liechtenstein, A. I., Anisimov, V. I. & Zaanen, J. Density-functional theory and strong interactions: Orbital ordering in mott-hubbard insulators. *Phys. Rev. B* **52**, R5467–R5470 (1995). URL <https://link.aps.org/doi/10.1103/PhysRevB.52.R5467>.
- [39] Nomoto, T. & Arita, R. Ab initio exploration of short-pitch skyrmion materials: Role of orbital frustration. *Journal of Applied Physics* **133** (2023).
- [40] Wills, J. M. & Cooper, B. R. Synthesis of band and model hamiltonian theory for hybridizing cerium systems. *Phys. Rev. B* **36**, 3809–3823 (1987). URL <https://link.aps.org/doi/10.1103/PhysRevB.36.3809>.
- [41] Wills, J., Eriksson, O., Alouani, M. & Price, D. “Full-Potential LMTO Total Energy and Force Calculations” in *Electronic structure and physical properties of solids* (Springer-Verlag Berlin Heidelberg, 2000). URL https://link.springer.com/chapter/10.1007/3-540-46437-9_4.
- [42] Wills, J. M. *et al.* *Full-Potential Electronic Structure Method: energy and force calculations with density functional and dynamical mean field theory*, vol. 167 (Springer Science & Business Media, 2010).
- [43] <https://www.physics.uu.se/research/materials-theory/ongoing-research/code-development/rspt-main/>. Source RSPt.

- [44] Liechtenstein, A., Katsnelson, M., Antropov, V. & Gubanov, V. Local spin density functional approach to the theory of exchange interactions in ferromagnetic metals and alloys. *Journal of Magnetism and Magnetic Materials* **67**, 65–74 (1987). URL <https://www.sciencedirect.com/science/article/pii/0304885387907219>.
- [45] Kvashnin, Y. O. *et al.* Exchange parameters of strongly correlated materials: Extraction from spin-polarized density functional theory plus dynamical mean-field theory. *Phys. Rev. B* **91**, 125133 (2015). URL <https://link.aps.org/doi/10.1103/PhysRevB.91.125133>.
- [46] Lichtenstein, A. I. & Katsnelson, M. I. Antiferromagnetism and d-wave superconductivity in cuprates: A cluster dynamical mean-field theory. *Phys. Rev. B* **62**, R9283–R9286 (2000). URL <https://link.aps.org/doi/10.1103/PhysRevB.62.R9283>.
- [47] Szilva, A. *et al.* Quantitative theory of magnetic interactions in solids. *Rev. Mod. Phys.* **95**, 035004 (2023). URL <https://link.aps.org/doi/10.1103/RevModPhys.95.035004>.
- [48] Daalderop, G. H. O., Kelly, P. J. & Schuurmans, M. F. H. First-principles calculation of the magnetocrystalline anisotropy energy of iron, cobalt, and nickel. *Phys. Rev. B* **41**, 11919–11937 (1990). URL <https://link.aps.org/doi/10.1103/PhysRevB.41.11919>.
- [49] Borisov, V. *et al.* Heisenberg and anisotropic exchange interactions in magnetic materials with correlated electronic structure and significant spin-orbit coupling. *Phys. Rev. B* **103**, 174422 (2021). URL <https://link.aps.org/doi/10.1103/PhysRevB.103.174422>.
- [50] Skubic, B., Hellsvik, J., Nordström, L. & Eriksson, O. A method for atomistic spin dynamics simulations: implementation and examples. *Journal of Physics: Condensed Matter* **20**, 315203 (2008). URL <https://dx.doi.org/10.1088/0953-8984/20/31/315203>.
- [51] Eriksson, O., Bergman, A., Bergqvist, L. & Hellsvik, J. *Atomistic Spin Dynamics: Foundations and Applications* (Oxford University Press, Oxford, UK, 2017).
- [52] Hellsvik, J. *et al.* General method for atomistic spin-lattice dynamics with first-principles accuracy. *Phys. Rev. B* **99**, 104302 (2019). URL <https://link.aps.org/doi/10.1103/PhysRevB.99.104302>.
- [53] Landau, L. & Lifshitz, E. 3 - on the theory of the dispersion of magnetic permeability in ferromagnetic bodies reprinted from physikalische zeitschrift der sowjetunion 8, part 2, 153, 1935. In PITAEVSKI, L. (ed.) *Perspectives in Theoretical Physics*, 51–65 (Pergamon, Amsterdam, 1992). URL <https://www.sciencedirect.com/science/article/pii/B9780080363646500089>.

- [54] Gilbert, T. A phenomenological theory of damping in ferromagnetic materials. *IEEE Trans. Mag.* **40**, 3443–3449 (2004).
- [55] Jensen, J. & Mackintosh, A. R. *Rare Earth Magnetism: Structures and Excitations* (Oxford University Press, 1991). URL <https://doi.org/10.1093/oso/9780198520276.001.0001>.
- [56] Loch, I. L. M. *et al.* Standard model of the rare earths analyzed from the hubbard i approximation. *Phys. Rev. B* **94**, 085137 (2016). URL <https://link.aps.org/doi/10.1103/PhysRevB.94.085137>.
- [57] Kvashnin, Y. O. *et al.* Microscopic origin of heisenberg and non-heisenberg exchange interactions in ferromagnetic bcc fe. *Phys. Rev. Lett.* **116**, 217202 (2016). URL <https://link.aps.org/doi/10.1103/PhysRevLett.116.217202>.
- [58] Sarkar, S. *et al.* Magnetism between magnetic adatoms on monolayer nbse₂. *2D Materials* **9**, 045012 (2022).
- [59] Sarkar, S., Sharma, S., Eriksson, O. & Di Marco, I. Understanding the nature of the magnetic coupling in transition metal doped bi₂se₃. *Phys. Rev. B* **110**, 064412 (2024). URL <https://link.aps.org/doi/10.1103/PhysRevB.110.064412>.
- [60] Yasui, Y. *et al.* Imaging the coupling between itinerant electrons and localised moments in the centrosymmetric skyrmion magnet gdru₂si₂. *Nature communications* **11**, 5925 (2020).
- [61] Hayami, S. & Motome, Y. Topological spin crystals by itinerant frustration. *Journal of Physics: Condensed Matter* **33**, 443001 (2021).
- [62] Khanh, N. D. *et al.* Zoology of multiple-q spin textures in a centrosymmetric tetragonal magnet with itinerant electrons. *Advanced Science* **9**, 2105452 (2022).
- [63] Hayami, S. & Motome, Y. Square skyrmion crystal in centrosymmetric itinerant magnets. *Physical Review B* **103**, 024439 (2021).
- [64] Garnier, A. *et al.* Anisotropic metamagnetism in gdru₂si₂. *Journal of magnetism and magnetic materials* **140**, 899–900 (1995).
- [65] Lin, Y., Grundy, P. & Giess, E. Bubble domains in magnetostatically coupled garnet films. *Applied Physics Letters* **23**, 485–487 (1973).
- [66] Garel, T. & Doniach, S. Phase transitions with spontaneous modulation-the dipolar ising ferromagnet. *Phys. Rev. B* **26**, 325–329 (1982). URL <https://link.aps.org/doi/10.1103/PhysRevB.26.325>.
- [67] Takao, S. A study of magnetization distribution of submicron bubbles in sputtered ho-co thin

- films. *Journal of magnetism and magnetic materials* **31**, 1009–1010 (1983).
- [68] Amoroso, D., Barone, P. & Picozzi, S. Spontaneous skyrmionic lattice from anisotropic symmetric exchange in a ni-halide monolayer. *Nature communications* **11**, 5784 (2020).
- [69] Momma, K. & Izumi, F. Vesta 3 for three-dimensional visualization of crystal, volumetric and morphology data. *Journal of Applied Crystallography* **44**, 1272–1276 (2011).
- [70] Qichen Xu, A. D., Olle Eriksson. Spinview: General interactive visual analysis tool for multiscale computational magnetism. *arXiv:2309.17367* (2023).